Energy Material Advances
A SCIENCE PARTNER JOURNAL

RESEARCH ARTICLE

# Modeling Silane Deposition in Nanoporous Carbon for High-Capacity Si/C Composite Anodes

**Zhinan Han[1], Joseph F. Wild[1], Justin J. Chen[2], and Yuan Yang[1]***

[1]Department of Applied Physics and Applied Mathematics, Columbia University, New York, NY 10027, USA. [2]John L. Miller Great Neck North High School, Great Neck, NY 11023, USA.

*Address correspondence to: yy2664@columbia.edu

**Citation:** Han Z, Wild JF, Chen JJ, Yang Y. Modeling Silane Deposition in Nanoporous Carbon for High-Capacity Si/C Composite Anodes. *Energy Mater. Adv.* 2024;5:Article 0111. https://doi.org/10.34133/energymatadv.0111

Submitted 9 May 2024
Accepted 1 July 2024
Published 28 August 2024



Si/nanoporous carbon composites are promising anode materials for high-energy-density lithium-ion batteries. Chemical vapor deposition of Si into nanoporous carbon is an efficient approach to synthesize high-performance Si/nanoporous carbon composites. While attractive performance has been demonstrated experimentally, there is a lack of modeling work to understand how experimental conditions and carbon properties affect deposition geometry and uniformity. This study aims to develop a general model of chemical vapor deposition of silicon into nanoporous carbon in a tube furnace, which describes key processes such as advection, diffusion, and reaction kinetics. Various parameters such as temperature, pressure, tube length, flow rate, surface area, and pore size were investigated to determine their effects on deposition uniformity and filling portion along the tube. The simulation results align with experimental results reasonably. The model predicts that lower temperature, lower pressure, higher flow rate, less carbon loading, and lower specific surface area favor better uniformity across the whole tube furnace. This work provides valuable insights for optimizing the operating conditions in tube reactors and can contribute to the advancement of deposition processes.

## Introduction

Rechargeable Li-ion batteries with high energy density are attractive for applications ranging from portable electronics to electric vehicles and grid-level energy storage [1–7]. Silicon has emerged as a promising anode candidate due to its high theoretical specific capacity of 4,200 mAh/g, which is about 10 times greater than that of graphite (372 mAh/g) [8–11]. However, the practical implementation of Si anodes is impeded by its large volume expansion (up to 300%) during lithiation, which leads to material pulverization and continuous solid–electrolyte interphase (SEI) formation, and thus fast capacity fading and short cycle life [12].

To mitigate these issues, various nanostructured Si electrodes have been proposed, such as Si nanowires [13–15], Si/nanocarbon particle composite [16,17], and Si nanotubes [18,19]. The nanostructures reduce volume expansion and material pulverization, and thus increase specific capacity and cycling performance [20]. However, nanostructures often have a remarkably higher surface area than micrometer-sized particles, which leads to low coulombic efficiency and reduces the energy density and cycle life of full cells, since the lithium source in full cells is limited. To reduce the surface area, micrometer-sized nanostructured Si anode has drawn more attention recently, which combines the advantages of micrometer-sized particles and nanostructures [21]. For example, Liu et al. [22] proposed a pomegranate-like assembly of carbon-coated Si nanoparticles, which shows a high capacity retention of 97% after 1,000 cycles and a reasonable initial Coulombic efficiency of 82%. However, the synthesis process is complicated for large-scale production.

Chemical vapor deposition (CVD) techniques have emerged as a promising strategy to realize high-performance Si anodes [23–27]. The direct CVD of Si into nanoporous carbon is particularly attractive due to its ability to tune the Si thickness and utilize the favorable conductivity and stability of carbon (Fig. 1A) [28,29]. In this design, the particle size of nanoporous carbon is 5 to 20 μm, which is good for increasing packing density and reducing surface area and thus SEI formation. On the other hand, the thickness of Si coating inside nanoporous carbon is only 1 to 2 nm, which helps dissipate stress inside. While improved performance has been reported, it is unclear how deposition conditions and pore structures affect deposition morphology, which is ultimately important for cycling performance.

In this paper, we target to develop a model to predict how the thickness and uniformity of Si deposition depends on deposition conditions and properties of nanoporous carbon. The model considers transport of silane ($SiH_4$) in both a tube furnace and nanoporous carbon particles, and the reaction kinetics of silane decomposition. We found that lower temperature, lower pressure, longer deposition zone, higher flow rate, and less carbon loading would give more uniform Si deposition. Carbon particles with smaller surface area and smaller pore volume also make Si deposition more uniform.

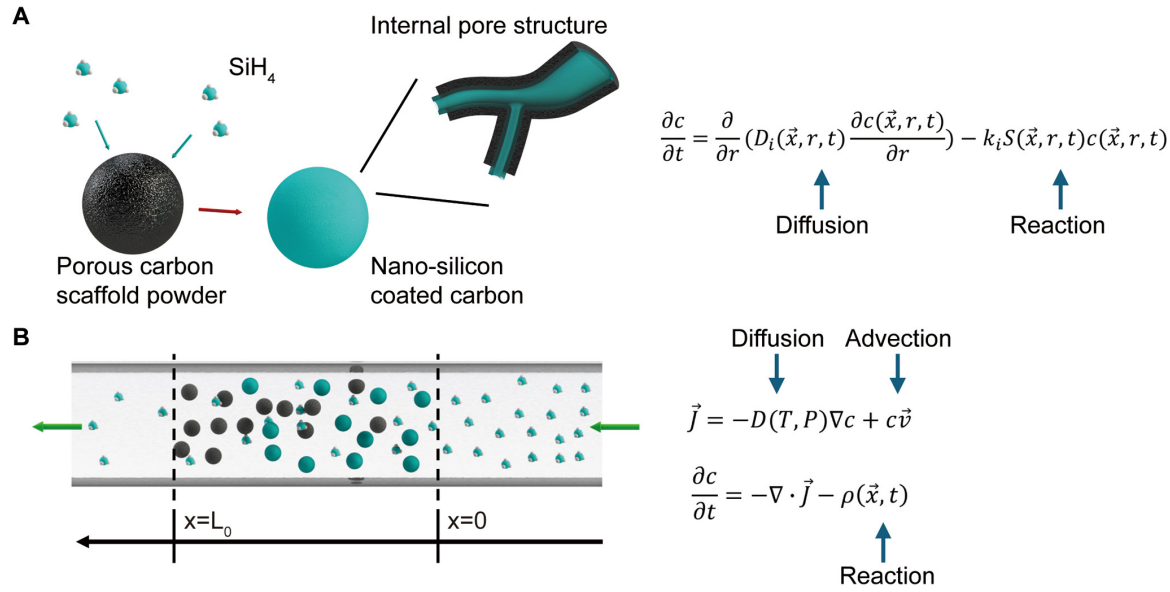


**Fig. 1.** (A) Schematic of silane decomposition into nanoporous carbon particles by a CVD process. Magnification shows the internal pore structure of the carbon particle. (B) Schematic of a tube furnace containing carbon powder with silane flowing from right to left. The middle region between 2 dashed lines represents the deposition zone.

## Methods

As shown in Fig. 1, the as-developed model takes 3 key transport processes into accounts: (a) transport of silane in a tube furnace, including both gas advection and diffusion; (b) diffusion of silane inside micrometer-sized nanoporous carbon particles; and (c) decomposition of silane to form solid silicon inside nanoporous carbon particles.

For transport in the tube furnace, the governing transport equations are

$$\vec{J} = -D(T,P)\nabla c + c\vec{v} \tag{1}$$

$$\frac{\partial c}{\partial t} = -\nabla \bullet \vec{J} - \rho(\vec{x},t) \tag{2}$$

where $\vec{J}$ is the molar flux of silane, $c$ is the silane concentration, $D$ is the diffusion coefficient of silane, $\vec{v}$ is the flow velocity of silane, and $\rho$ is the consumption rate of silane. The velocity is controlled by the gas flow through a flowmeter. The temperature ($T$)- and pressure ($P$)-dependent $D$ is taken into account, which is expressed as $D = \frac{(T/T_0)^{\frac{3}{2}}}{P/P_0} D_0$, where $P_0$ is $1.01 \times 10^5$ Pa and $T_0$ is 298.15 K. $D_0$ is the diffusivity of silane at $P_0$ and $T_0$, which is set to $0.2 \times 10^{-4}$ m$^2$/s. The derivation is shown in Section S1. The boundary condition is $J(\vec{x},r,t)\big|_{x_1=-L_1} = (c_0 v 0)$, $\frac{\partial c}{\partial x_1}\Big|_{x_1=L_0} = 0$, and the initial condition is $c(\vec{x},r,0) = c_0$, where $L_1$ is the distance between the gas source and the start of the deposition zone, $L_0$ is the deposition zone length, and $c_0$ is the concentration of silane at the gas source.

For transport inside a microparticle of nanoporous carbon, there is no advection as the pore size is nanoscale, and the only process is diffusion in pores. Moreover, the transport process is independent of polar angle and azimuthal angle, so the governing equation is

$$\frac{\partial c(\vec{x},r,t)}{\partial t} = \frac{\partial}{\partial r}\left(D_i(\vec{x},r,t)\frac{\partial c(\vec{x},r,t)}{\partial r}\right) - k_i S(\vec{x},r,t)c(\vec{x},r,t) \tag{3}$$

The boundary condition is $\frac{\partial c}{\partial r}\Big|_{r=0} = 0$ and the initial condition is $c(\vec{x},r,0) = c_0$, where $D_i$ is the diffusion coefficient inside the particle, $k_i$ is the consumption rate of silane, $S$ is the surface area per volume of porous carbon, and $r_0$ is the radius of the particle. At the target deposition temperature and pressure, the mean free path ($\lambda_0$) of silane gas is ~10 to 100 nm, which is much larger than the pore size. Therefore, a modified Knudsen diffusion model is used to correct the diffusivity (Section S2). Moreover, as silane diffuses into the porous matrix, we applied the Buggerman theory to take porosity and tortuosity into account, which yields

$$D_i(\vec{x},r,t) = \varepsilon(\vec{x},r,t)^{\frac{3}{2}} A \frac{D}{\lambda_0} w(\vec{x},r,t) \tag{4}$$

where $\varepsilon$ is the time-dependent porosity of a carbon particle and $w$ is the time-dependent pore diameter in carbon particles. $A$ is the correction factor that takes molecule–wall interactions into account. To account for gradual silane deposition, $w(\vec{x},r,t) = w_0 - 2H(\vec{x},r,t)$, where $w_0$ is the initial pore diameter and $H$ is the thickness of deposited silicon. $S(\vec{x},r,t) = \left(\frac{w(\vec{x},r,t)}{w_0}\right)^2 S_0$, where $S_0$ is the initial surface area.

The transport in the tube furnace (Eqs. 1 and 2) and the transport inside porous carbon particles (Eq. 3) are coupled by the reaction rate of silane decomposition. For coupling of the silane reaction rate, the reaction rate at a location $(\vec{x}, r)$ in the tube furnace ($\rho$) equals the Si deposition in all particles at this location, which is

$$\rho(\vec{x},t) = \rho_i(\vec{x},t) + \rho_o(\vec{x},t) \tag{5}$$

$$\rho_i(\vec{x},t) = p\int k_i S(\vec{x},r,t)c(\vec{x},r,t)dV / V_{par} \quad (6)$$

$$\rho_o(\vec{x},t) = 3pk_o c(\vec{x},r_0,t) / r_0 \quad (7)$$

where $\rho_i$ is the reaction rate inside the particle; $\rho_o$ is the reaction rate on the surface of the particle; $p$ is the volume fraction of carbon particles to the reactor volume; $k_i$ and $k_o$ are the deposition rate inside and on the surface of the particle, respectively; and $V_{par}$ is the volume of a particle, which equals $\frac{4}{3}\pi r_0{}^3$. The integral in $\rho_i$ is over an entire particle.

## Results

### Simulation Results and Experimental Verification

To validate that the model can describe experimental results semiquantitatively, we first use temperature-dependent deposition time, radial uniformity inside a nanoporous particle, and tubing position-dependent Si deposition percentage as validation of intraparticle and interparticle distributions. Deposition temperatures of 485 and 535 °C are chosen, which are in a typical range for silicon deposition. When the temperature is larger than 550 °C, substantial self-nucleation of silicon nanoparticles occurs (Fig. S4B), which impedes uniform Si deposition [30]. When the temperature is less than 450 °C, the silane decomposition rate is too low to be practical.

In the corresponding experiment, 2% silane in $N_2$ is pumped into a tube furnace with a deposition zone ($L_0$) of 8 cm and a uniform distribution of carbon particles of 0.2 g inside this deposition zone. The total gas pressure is 0.8 atm, and the flow rate is 150 $cm^3$/min. The parameters of carbon particles are based on properties of those used in experimental validation, which have a median radius of 6 μm (Fig. S4A and B). Brunauer–Emmett–Teller (BET) measurements show that the surface area is 1,712 $m^2$/g and the peak pore size is 1.85 nm. These parameters are used in all simulations.

In the simulation results (Fig. 2A), it takes 62.2 and 42.4 min at 485 and 535 °C, respectively, to reach an overall Si wt % (Si/Si + C) of 40%, which is a typical target for Si/C composite anodes. This is because higher temperature renders faster deposition. The simulated time semiquantitatively align with experimental results, which are 60 min at 485 °C and 45 min at 535 °C, respectively. Such results indicate the validity of the model.

The model also captures the zone position ($x_1$)-dependent silicon deposition at different temperatures (Fig. 2B). At 485 °C, the model shows that Si wt % is moderately uniform inside the tube, decreasing from 45.6% at the beginning of the deposition zone ($x_1 = 0$) to 33.1% at the end of deposition zone ($x_1 = L_0$). At 535 °C, the model shows less uniformity and Si wt % varies from 50.0% to 27.0% along the deposition zone. Such results also align qualitatively with experimental observation (Section S6).

We further studied the temperature-dependent intraparticle uniformity. In simulation results (Fig. 3E and F), when the overall Si wt % reaches 40%, the intraparticle Si deposition is highly uniform at 485 °C. The ratio of deposited Si thickness ($H$) at $r = 0$ and $r = r_0$ ($H_0/H_{r0}$) is 0.98. The corresponding ratio of deposited Si wt % ($WP$) at $r = 0$ and $r = r_0$ ($WP_0/WP_{r0}$) is 0.99. These results indicate excellent uniformity. When the temperature increases to 535 °C, uniformity was still observed, where $H_0/H_{r0}$ is 0.97 and $WP_0/WP_{r0}$ is 0.99.

Such simulation results are consistent with experimental observations by cross-sectional energy-dispersive x-ray spectroscopy (EDS) mapping of Si in focused ion beam (FIB)-cut Si/C particles after silane deposition (Fig. 3A and B), with corresponding scanning electron microscopy (SEM) images (Fig. 3C and D). First, EDS mapping results show uniform Si deposition in nanoporous carbon particles at 485 and 535 °C. Moreover, quantitative EDS analysis (Fig. 3G) also shows a similar homogeneity as modeling results. For example, $WP_0/WP_{r0}$ of 1.05 and 1.02 were observed at 485 and 535 °C, respectively.

Moreover, we also investigated the effects of pressure and zone length (Section S9). The simulation results also align with the experiments. Overall, the model prediction aligns with experimental results.



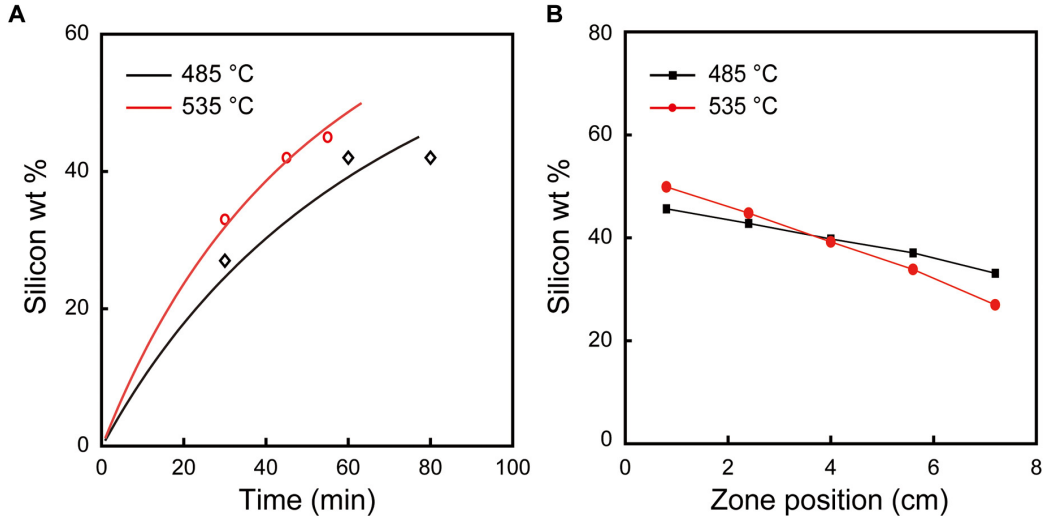


**Fig. 2.** (A) Simulated and experimental Si wt % versus time at 485 and 535 °C, where simulation results are lines and experimental results are symbols. (B) Simulated silicon weight portion versus zone position at 485 and 535 °C.

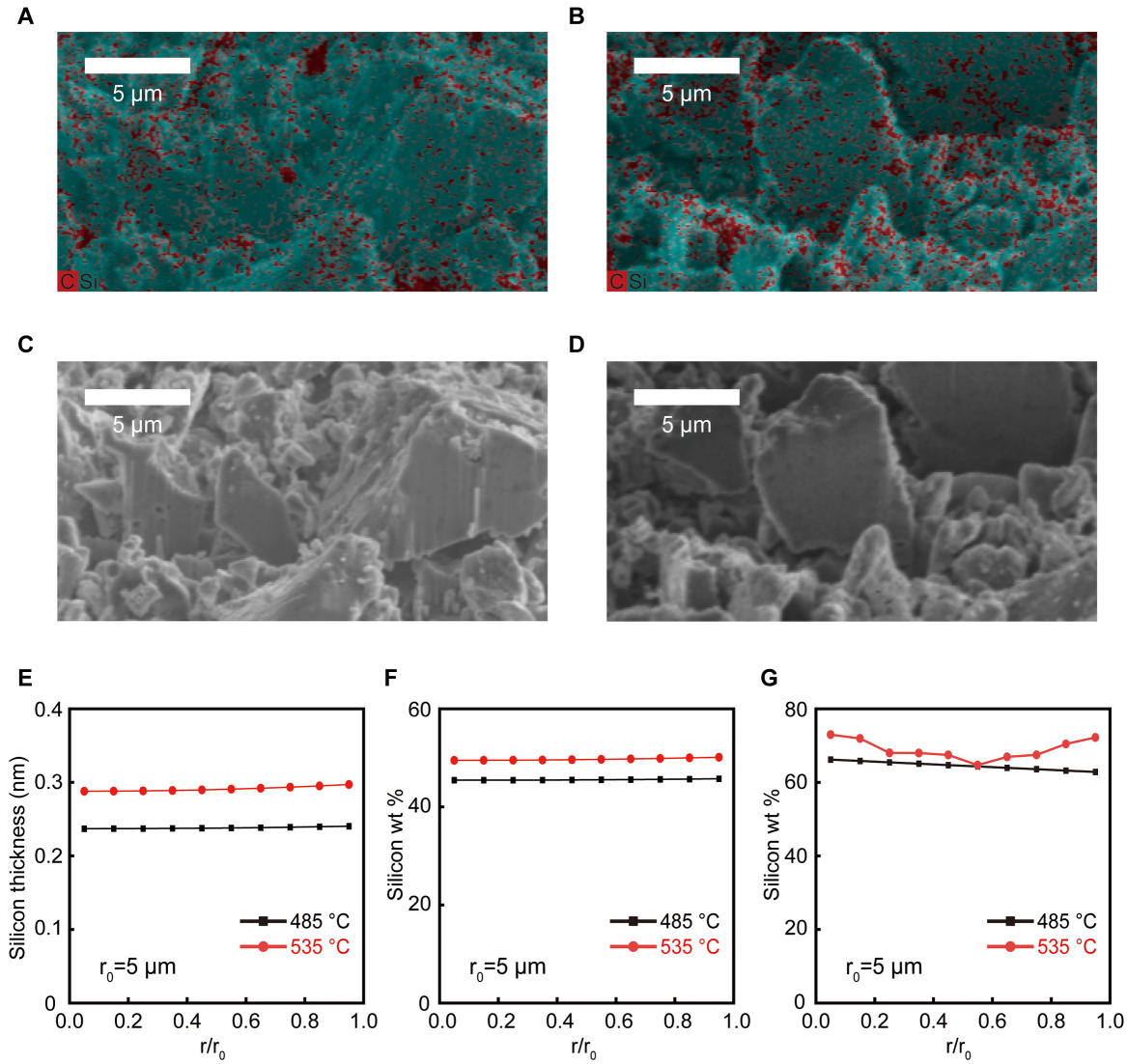


**Fig. 3.** (A and B) EDS mapping results of carbon particles after silane deposition at 485 and 535 °C. (C and D) SEM results of carbon particles after silane deposition at 485 and 535 °C. (E) Simulated deposition thickness ($H$) versus normalized radius ($r/r_0$) for particles at 485 and 535 °C. (F) Simulated silicon weight portion versus normalized radius at 485 and 535 °C. (G) Experimental results of silicon weight portion versus normalized radius at 485 and 535 °C.

## Modeling Prediction

### *Effects of deposition conditions*

After validating our model by experiments, we carried out further simulations to understand the effects of various parameters on Si deposition, including pressure, flow rate, carbon loading, and deposition zone length. In this section, we focus on a larger tube furnace with a diameter of 30 cm, which can accommodate more carbon powders (e.g., 10 to 100 g). Such scale can be used for small-scale pilot production in industry. The baseline condition is 485 °C, 0.8 atm, 0.1 m deposition zone length, 50 l/min flow rate, and 50 g carbon loading. More model parameters can be found in Table S2. Forty percent of overall Si wt % and uniform deposition are targeted for high-performance anodes. Among different parameters, we find that lower pressure, longer deposition zone length, higher flow rate, and less carbon loading favor better deposition uniformity. The details are as follows. It should be noted that these simulation results need to be experimentally verified in the future.

We first studied pressures in the range of 0.2 to 2 atm, which are practical for industrial applications. First, we observe that a lower pressure leads to a lower overall deposition rate (Fig. 4A). At 0.2 atm, it takes 17.4 min to reach 40%, while at 2 atm, the deposition time is only 4.7 min. This is because a higher pressure leads to a higher concentration of silane, thus a higher deposition rate. On the other hand, a lower pressure results in more uniform deposition along the tube (Fig. 4B). At 0.2 atm, Si wt % is 42.4% at $x_1 = 0$ to 37.2% at $x_1 = 10$ cm. When the pressure increases to 2 atm, Si wt % is 56.3% at $x_1 = 0$, which decreases to 18.1% at $x_1 = 10$ cm. This is because a lower pressure leads to a higher flow of silane so silane can reach the downstream of the tube more easily to enable more uniform deposition. Along with the dependence of Si wt % on zone position, the pressure has little effect on intraparticle uniformity (Fig. 4C). This indicates that the intraparticle uniformity is insensitive to pressure at 485 °C.

Next, we studied the effect of deposition zone length ($L$) in the range of 0.05 to 0.4 m. First, zone length has little effect on the overall deposition rate (Fig. 4D), and it takes 6.5 min to reach 40% for all $L$. As shown in Fig. 4E, when Si wt % averages 40% inside all particles, the Si deposition shows best uniformity along the tube when $L = 0.4$ m. Si wt % is 47.1% at $x_1 = 0$ to 31.8% at

$x_1$= 40 cm. When $L$ decreases to 0.05 m, Si wt % is less uniform, which is 48.8% at $x_1$= 0 to 29.1% at $x_1$= 5 cm. This is because a longer tube means less carbon loading per unit length; thus, more silane will reach downstream to enable better uniformity. The intraparticle uniformity is also almost the same at different $L$ (Fig. 4F). This is because the intraparticle uniformity is mainly determined by the competition of reaction rate ($k_i$) and diffusivity ($D_i$), so zone length has little effect on the uniformity.

We further studied the effect of total flow rates in the range of 20 to 100 l/min with a fixed silane flow rate of 10 l/min, and we found that a lower flow rate leads to a faster deposition (Fig. 4G). At 100 l/min, it takes 10.1 min to reach 40 wt % Si deposition, and at 20 l/min, the deposition time is reduced to 4.4 min. This is because when the silane flow rate is fixed, a higher total flow rate gives a higher velocity of silane, making it easier to leave the deposition zone. Therefore, less silane is consumed in the deposition zone, and thus, it takes longer to reach 40%. The best uniformity along the tube is achieved when the flow rate is 100 l/min (Fig. 4H). Si wt % is 44.8% at $x_1$ = 0 to 33.9% at 100 l/min, and Si wt % is 54.1% at $x_1$ = 0 to 23.4% at $x_1$ = 10 cm at 20 l/min. This is because a higher flow rate results in a higher velocity for silane, making it easier to reach downstream for more uniform deposition. The intraparticle uniformity (Fig. 4I) is also unaffected by the flow rates due to the low deposition temperature of 485 °C.

Finally, we studied carbon loadings in the range of 25 to 100 g. As shown in Fig. 4J, it takes 5.1 min to reach Si wt % of 40% at 25-g carbon load. As more carbon is loaded, the overall deposition rate decreases. The deposition time is 9.7 min at 100-g carbon load. This is because Si is deposited relatively slower at a higher carbon loading, leading to a lower deposition rate. A smaller carbon loading favors a more uniform deposition along the tube (Fig. 4K). At 25 g, Si wt % is 44.7% at $x_1$= 0 to 34.4% at $x_1$= 10 cm. When the loading increases to 100 g, Si wt % is 54.2% at $x$= 0 to 21.2% at $x_1$= 10 cm. This is because at a low carbon loading, more silane would reach downstream to enable uniformity since it is less consumed at the upstream. The same as other parameters, excellent intraparticle uniformity is still observed at both 25- and 100-g loading (Fig. 4L)

### *Effects of carbon properties*

Besides deposition conditions, pore properties also affect deposition substantially, such as specific surface area (*SSA*), pore volume, and pore size. We find that larger *SSA*, smaller pore volume gives better deposition, while pore size does not show noticeable influence. The details are listed below. If not specified, all data (e.g., deposition time and Si wt % distribution) are at the moment when the overall Si wt % is 40%.

We first studied the effect of *SSA* in the range of 500 to 2,000 $m^2$/g, which is common for nanoporous carbon. As shown in Fig. 5A, a larger *SSA* leads to a longer deposition time. At 500 $m^2$/g, the deposition time is 4.6 min. As *SSA* increases to 2,000 $m^2$/g, the deposition time increases to 7.6 min. This is because a smaller *SSA* leads to less silane consumption at the upstream, enabling more silane to reach downstream to have a higher overall deposition rate. A larger *SSA* also leads to less uniform deposition along the tube (Fig. 5B). At 500 $m^2$/g, Si wt % is 43.3% at $x_1$= 0 to 36.2% at $x_1$= 10 cm. As *SSA* increases to 2,000 $m^2$/g, Si wt % is 50.7% at $x_1$= 0 to 26.3% at $x_1$= 10 cm. This is because the silane consumption rate is proportional to *SSA*, and thus, less silane can penetrate into the downstream at a higher *SSA*, leading to poorer uniformity. On the other hand, *SSA* has little effect on the intraparticle uniformity (Fig. 5C). At 500 and 2,000 $m^2$/g, $H_0/H_{r0}$ are 0.996 and 0.986 at the middle of the deposition zone, respectively.

Next, we studied pore volumes in the range of 0.5 to 1.5 $cm^3$/g. A larger pore volume leads to a faster overall deposition (Fig. 5D). At 0.5 $cm^3$/g, the deposition time is 9.9 min, while at 1.5 $cm^3$/g, the deposition time is 3.3 min. This is because a larger pore volume gives smaller $S$, which leads to less silane consumption at the upstream, enabling more silane to reach downstream to have a higher overall deposition rate. A larger pore volume also leads to less uniform deposition along the tube (Fig. 5E). At a pore volume of 0.5 $cm^3$/g, Si wt % is 46.6% at $x_1$= 0 to 31.3% at $x_1$= 10 cm. At 1.5 $cm^3$/g, Si wt % is 50.3% at $x_1$= 0 to 27.7% at $x_1$= 10 cm. This arises from that a larger pore volume leads to a larger volume fraction ($P$) of carbon particles in the tube furnace, which would increase the consumption rate of silane, so less silane would reach downstream, which reduces uniformity. Excellent intraparticle uniformity is still observed at different pore volumes (Fig. 5F) due to the low deposition temperature of 485 °C.

Finally, we studied pore sizes in the range of 1 to 2 nm, which is common for nanoporous carbon. First, a smaller pore size leads to a larger overall deposition rate (Fig. 5G). At 1 nm, the deposition time is 4.4 min, while at 2 nm, the deposition time increases to 8.7 min. This is because a smaller pore size means higher silicon Si wt % at the same deposition thickness ($H$), which leads to a higher deposition rate. The uniformity along the tube is essentially the same, and Si wt % is 48.5% at $x_1$= 0 to 29.3% at $x_1$= 10 cm (Fig. 5H). However, the intraparticle uniformity is slightly affected (Fig. 5I). At 1 nm, $H_0/H_{r0}$ is 0.984 at the middle of the deposition zone. At 2 nm, $H_0/H_{r0}$ is 0.992 at the middle of the deposition zone. This is because small pores render much lower diffusivities than large pores, which limit the deep penetration of silane into such nanopores.

## Discussion

Based on the analysis above, we can see that a major challenge in achieving uniform large-scale deposition of Si in a tube furnace is the nonuniformity across the deposition zone, which arises from consumption of silane at the upstream of the deposition zone and thus lower silane concentration at the downstream. To avoid this, we propose 2 strategies. The first one is to have exchange between carbon particles upstream and downstream, which can be realized by fluidized bed-based CVD [31] (Fig. S6A). The second one is to have a concentric tubing design, where silane flows in the inner tube and carbon powders are in the outer tube. The silane flows onto carbon powders by openings on the inner tube (Fig. S6B).

In summary, we successfully created a model to describe the transport of silane gases in a tube furnace and pores of nanoporous carbon, where convection, diffusion, and reaction kinetics were taken into account. The modeling results show a reasonable degree of consistency with experimental results in a laboratory-scale tube furnace. After approving the validity of the model, we further used it to predict the effect of different experimental parameters and carbon properties on the deposition uniformity. We found that at 485 °C, lower pressure, longer deposition zone, higher flow rate, and less carbon loading favor uniform deposition across the whole deposition zone. Meanwhile, these parameters have little effect on the intraparticle uniformity, and the intraparticle uniformity is always very good. This is attributed

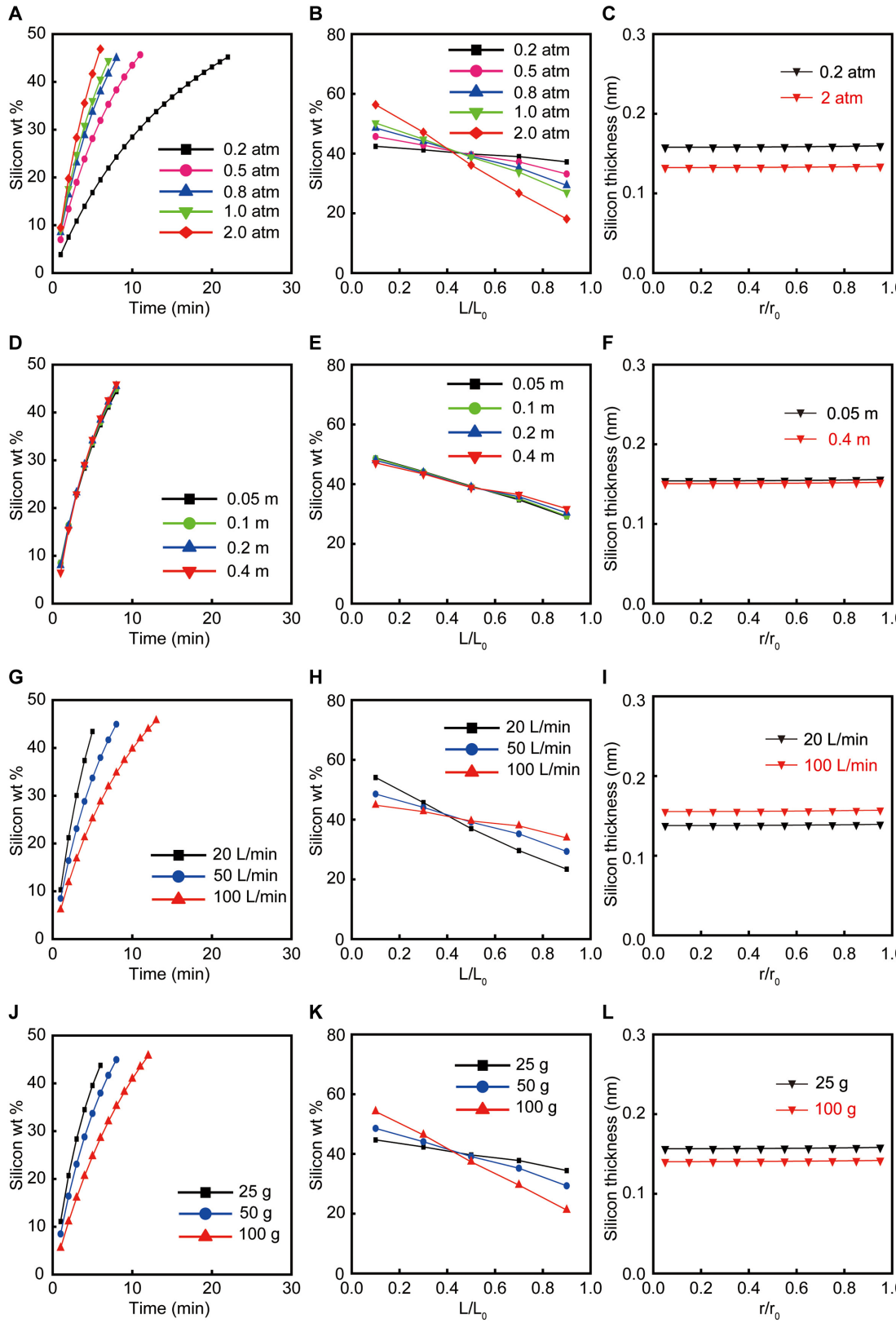


**Fig. 4.** (A to C) Modeling prediction of (A) deposited Si wt % versus time, (B) deposited Si wt % versus normalized zone position ($L/L_0$), and (C) deposited Si thickness ($H$) versus normalized particle radius ($r/r_0$) at the middle of the tube between pressure of 0.2 and 2 atm. (D to F) Modeling prediction of (D) deposited Si wt % versus time, (E) deposited Si wt % versus normalized zone position ($L/L_0$), and (F) deposited Si thickness ($H$) versus normalized particle radius ($r/r_0$) at the middle of the tube between zone length of 0.05 and 0.4 m. (G to I) Modeling prediction of (G) deposited Si wt % versus time, (H) deposited Si wt % versus normalized zone position ($L/L_0$), and (I) deposited Si thickness ($H$) versus normalized particle radius ($r/r_0$) at the middle of the tube between flow rate of 20 and 100 l/min. (J to L) Modeling prediction of (J) deposited Si wt % versus time, (K) deposited Si wt % versus normalized zone position ($L/L_0$), and (L) deposited Si thickness ($H$) versus normalized particle radius ($r/r_0$) at the middle of the tube between carbon loading of 25 and 100 g.

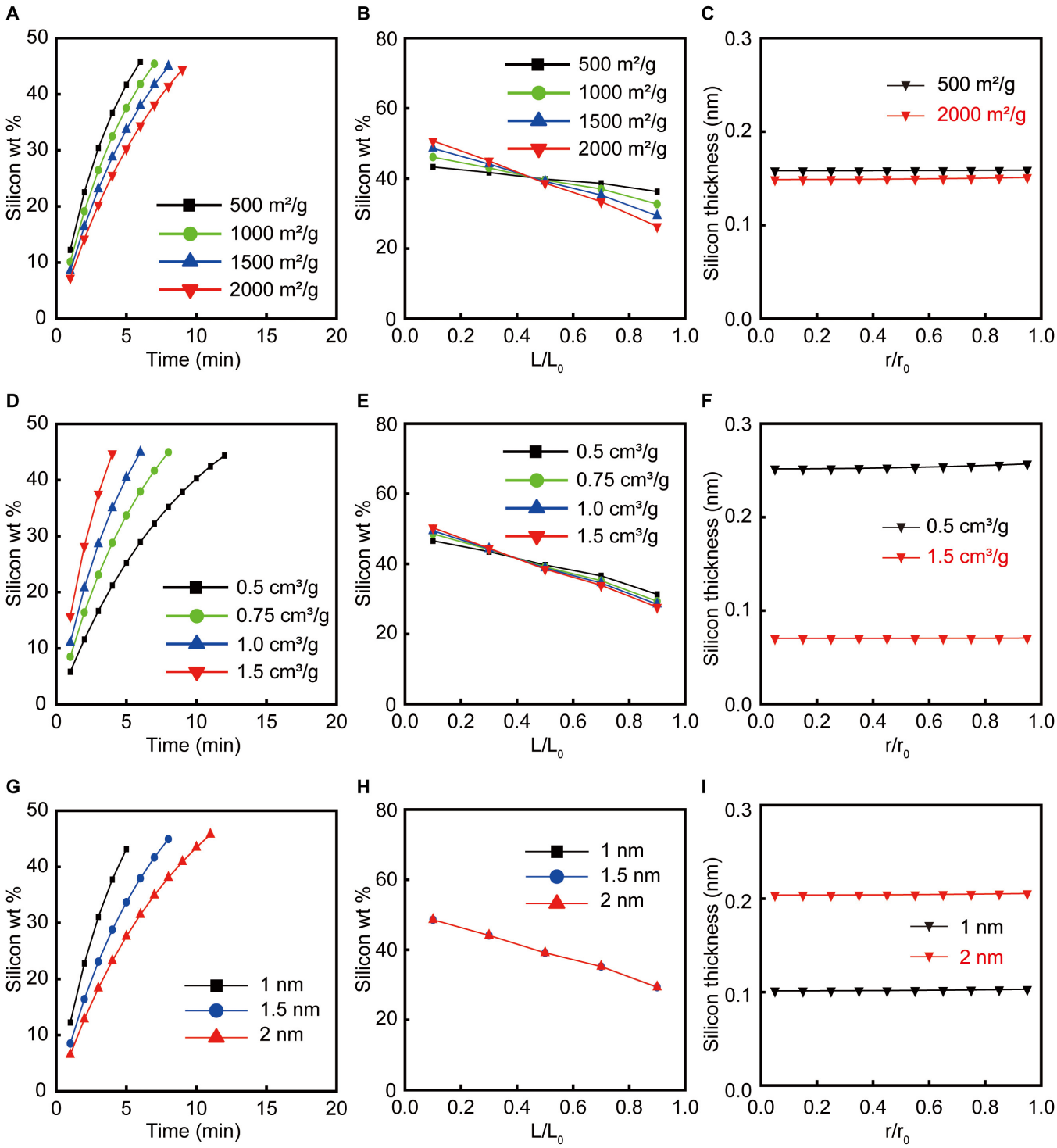


**Fig. 5.** (A to C) Modeling prediction of (A) deposited Si wt % versus time, (B) deposited Si wt % versus normalized zone position ($L/L_0$), and (C) deposited Si thickness ($H$) versus normalized particle radius ($r/r_0$) at the middle of the tube between surface area of 500 and 2,000 $m^2/g$. (D to F) Modeling prediction of (D) deposited Si wt % versus time, (E) deposited Si wt % versus normalized zone position ($L/L_0$), and (F) deposited Si thickness ($H$) versus normalized particle radius ($r/r_0$) at the middle of the tube between pore volume of 0.5 and 1.5 $cm^3/g$. (G to I) Modeling prediction of (G) deposited Si wt % versus time, (H) deposited Si wt % versus normalized zone position ($L/L_0$), and (I) deposited Si thickness ($H$) versus normalized particle radius ($r/r_0$) at the middle of the tube between pore size of 1 and 2 nm.

to the fact that at 485 °C, the reaction rate is much smaller than the diffusion rate in nanoporous carbon. On the other hand, lower surface area and lower pore volume can improve deposition uniformity across the whole deposition zone, while the pore size is insignificant to the uniformity.

## Acknowledgments

**Funding:** This work was supported in part by Gotion Inc.
**Author contributions:** Y.Y. and Z.H. formulated the model. Z.H. wrote the code and performed the simulations. J.F.W. performed the experiments and characterization. Z.H., J.F.W., and

Y.Y. wrote the manuscript. All authors contributed to data analysis. Y.Y. supervised the project.
**Competing interests:** The authors declare that they have no competing interests.

## Data Availability

All data are available in the manuscript or the Supplementary Materials. Information requests should be directed to the corresponding author.

## Supplementary Materials

Sections S1 to S9
Figs. S1 to S7
Tables S1 and S2
References

## References


1. Scrosati BaG J. Lithium batteries: Status, prospects and future. *J Power Sources*. 2010;195:2419–2430.
2. Armand M, Tarascon J-M. Building better batteries. *Nature*. 2008;451(7179):652–657.
3. Liu C, Li F, Ma L-P, Cheng HM. Advanced materials for energy storage. *Adv Mater*. 2010;22(8):E28–E62.
4. Whittingham MS. Lithium batteries and cathode materials. *Chem Rev*. 2004;104(10):4271–4302.
5. Tarascon JM, Armand M. Issues and challenges facing rechargeable lithium batteries. *Nature*. 2001;414(6861):359–367.
6. Yang Y, Jeong S, Hu L, Wu H, Lee SW, Cui Y. Transparent lithium-ion batteries. *Proc Natl Acad Sci U S A*. 2011;108(32):13013–13018.
7. Li M, Lu J, Chen Z, Amine K. 30 years of lithium-ion batteries. *Adv Mater*. 2018;30(33):1800561.
8. Bourderau S, Brousse T, Schleich DM. Amorphous silicon as a possible anode material for Li-ion batteries. *J Power Sources*. 1999;81–82:233–236.
9. Dong H, Wang J, Ding H, Zong F, Wang P, Song R, Zhang N, Cui X, Cui X, Li S. Exploring the practical applications of silicon anodes: A review of silicon-based composites for lithium-ion batteries. *Ionics*. 2022;28(7):3057–3077.
10. Li H, Li H, Lai Y, Yang Z, Yang Q, Liu Y, Zheng Z, Liu Y, Sun Y, Zhong B, et al. Revisiting the preparation progress of nano-structured Si anodes toward industrial application from the perspective of cost and scalability. *Adv Energy Mater*. 2022;12(7):2102181.
11. Zhang Y, Wu B, Mu G, Ma C, Mu D, Wu F. Recent progress and perspectives on silicon anode: Synthesis and prelithiation for LIBs energy storage. *J Energy Chem*. 2022; 64:615–650.
12. Zhang JG, Wang W, Xiao J, Xu W, Graff GL, Yang G, Choi D, Wang D, Li X, Liu J. Silicon-based anodes for Li-ion batteries. In: Meyers RA, editor. *Encyclopedia of sustainability science and technology*. New York (NY): Springer; 2012.
13. Li-Feng Cui YY, Hsu C-M, Cui Y. Carbon–silicon core–shell nanowires as high capacity electrode for lithium ion batteries. *Nano Lett*. 2009;9(9):3370–3374.
14. Boukai A, Bunimovich Y, Tahir-Kheli J, Yu JK, Goddard III WA, Heath JR. Silicon nanowires as efficient thermoelectric materials. *Nature*. 2008;451(7175):168–171.
15. Chan C, Peng H, Liu G, McIlwrath K, Zhang XF, Huggins RA, Cui Y. High-performance lithium battery anodes using silicon nanowires. *Nat Nanotechnol*. 2008;3:31–35.
16. Xu H, Ding M, Li D, Liu Y, Jiang Y, Li F, Xue B. Silicon nanoparticles coated with nanoporous carbon as a promising anode material for lithium ion batteries. *New J Chem*. 2020;44(40):17323–17332.
17. Kwon HJ, Hwang J-Y, Shin H-J, Jeong M-G, Chung KY, Sun Y-K, Jung H-G. Nano/microstructured silicon–carbon hybrid composite particles fabricated with corn starch biowaste as anode materials for Li-ion batteries. *Nano Lett*. 2019;20(1):625–635.
18. Park M-H, Kim MG, Joo J, Kim K, Kim J, Ahn S, Cui Y, Cho J. Silicon nanotube battery anodes. *Nano Lett*. 2009;9(11): 3844–3847.
19. Wen Z, Lu G, Mao S, Kim H, Cui S, Yu K, Huang X, Hurley PT, Mao O, Chen J. Silicon nanotube anode for lithium-ion batteries. *Electrochem Commun*. 2013;29:67–70.
20. Szczech JR, Jin S. Nanostructured silicon for high capacity lithium battery anodes. *Energy Environ Sci*. 2011;4(1):56–72.
21. Wu M, JEC S, Song X, Minor AM, Battaglia VS, Liu G. In situ formed Si nanoparticle network with micron-sized Si particles for lithium-ion battery anodes. *Nano Lett*. 2013;13(11): 5397–5402.
22. Liu N, Lu Z, Zhao J, McDowell MT, Lee HW, Zhao W, Cui Y. A pomegranate-inspired nanoscale design for large-volume-change lithium battery anodes. *Nat Nanotechnol*. 2014;9(3):187–192.
23. Lee C-Y, Yeh F-H, Yu I-S. A commercial carbonaceous anode with a-Si layers by plasma enhanced chemical vapor deposition for lithium ion batteries. *J Compos Sci*. 2020;4(2):72.
24. Hu M, Wu H, Zhang G-J. High-performance silicon/graphite anode prepared by CVD using SiCl4 as precursor for Li-ion batteries. *Chem Phys Lett*. 2023;833:140917.
25. Liu B, Huang P, Xie Z, Huang Q. Large-scale production of a silicon nanowire/graphite composites anode via the CVD method for high-performance lithium-ion batteries. *Energy Fuel*. 2021;35(3):2758–2765.
26. An W, He P, Che Z, Xiao C, Guo E, Pang C, He X, Ren J, Yuan G, du N, et al. Scalable synthesis of pore-rich Si/C@C core–shell-structured microspheres for practical long-life lithium-ion battery anodes. *ACS Appl Mater Interfaces*. 2022;14(8):10308–10318.
27. Song H, Zhang X, Ye J, Yang Y, Sun D, Xu C, Lin R, Zhang X, Zhang M, Li S, et al. Si@graphene composite anode with high capacity and energy density by fluidized chemical vapor deposition. *Chem Eng Sci*. 2023;274:118706.
28. Yang J, Kahn H, He A-Q, Phillips SM, Heuer AH. A new technique for producing large-area as-deposited zero-stress LPCVD polysilicon films: The MultiPoly process. *J Microelectromech Syst*. 2000;9(4):485–494.
29. Ko M, Chae S, Ma J, Kim N, Lee HW, Cui Y, Cho J. Scalable synthesis of silicon-nanolayer-embedded graphite for high-energy lithium-ion batteries. *Nat Energy*. 2016;1(9):16113.
30. Onischuk A, Panfilov VN. Mechanism of thermal decomposition of silanes. *Russ Chem Rev*. 2001;70:321–332.
31. Coppey N, Noé L, Monthioux M, Caussat B. Fluidized bed chemical vapor deposition of silicon on carbon nanotubes for Li-ion batteries. *J Nanosci Nanotechnol*. 2011;11(9): 8392–8395.